Multi-scale experimental study of trapped gas mobilization in carbonate rocks

Dev Joshi*, *Ziqiang* Qin, *Amir H.* Alizadeh, and *Mohammad* Piri

Center of Innovation for Flow through Porous Media, Department of Energy and Petroleum Engineering, University of Wyoming, Laramie, WY 82071, USA

Abstract. During the displacement of the non-wetting phase by the wetting phase in porous rocks, a fraction of the non-wetting phase may become hydraulically disconnected due to capillary forces. Mobilization of this trapped phase could occur when viscous forces overcome the capillary forces, with the threshold for mobilization being approximated by the capillary number, N_{ca} (the ratio of viscous to capillary forces). In liquid-liquid systems within sandstone rocks, non-wetting phase saturation remains relatively stable as viscous forces increase, until a threshold N_{ca} (typically ranging from 10^{-6} to 10^{-4}) is reached. Once this threshold is surpassed, mobilization of the trapped non-wetting phase commences, leading to a gradual (or sometimes sharp) decline in non-wetting phase saturation. However, for gas-liquid systems, there is evidence that gas phase mobilization occurs at much lower N_{ca} than those observed for liquid-liquid systems in sandstones, with this effect being particularly pronounced in carbonates due to their more complex pore structures. Despite various hypotheses, the applicability of the threshold N_{ca} to gas-liquid systems remains debated, highlighting a gap in the understanding of gas mobilization mechanisms in porous media. In this study, we investigated the mobilization of trapped gas in carbonate rocks through a series of high-pressure, high-temperature coreflooding experiments using a nitrogen-brine fluid system. Experiments were conducted at both micro and macro scales, incorporating x-ray imaging to generate in-situ data on gas mobilization and distribution mechanisms. A diverse suite of carbonate rocks, including both outcrop and reservoir samples, was employed to encompass a broad range of petrophysical properties and pore-throat size distributions. To assess the influence of dynamic forces on trapped gas saturation, we systematically increased the brine flow rate during waterflood experiments following the establishment of initial water saturation through drainage. Our results demonstrate a clear, continuous decrease in trapped gas saturation with increasing brine flow rates, even within the so-called capillary-dominated flow regime. High-resolution x-ray imaging provided valuable insights into the gas displacement mechanisms, revealing the mobilization and redistribution of trapped gas within the intricate pore networks of carbonate rocks. Specifically, the in-situ data showed fragmentation and subsequent mobilization of trapped gas ganglia with increasing flow rates. These findings suggest that the conventional threshold N_{ca} values – derived from well-established equations in the literature – may not sufficiently account for gas mobilization behavior in carbonate rocks, highlighting the need for a deeper understanding of the mechanisms driving gas movement in complex rocks.

1 Introduction

Accurate assessment of reservoir performance techniques necessitates the quantification of residual non-wetting phase saturation (S_{nwr}), which denotes the hydraulically isolated and immobile fluid saturation after waterflooding operations. The phenomenon of non-wetting phase entrapment is governed by the complex interaction between viscous and capillary forces. Capillary forces, arising from interfacial tension at fluid-fluid interfaces hinder the displacement of the non-wetting phase and contribute to its entrapment. Conversely, viscous forces, generated by pressure gradients during fluid flow, act to overcome capillary resistance, facilitating fluid displacement and reducing the extent of trapping. The relative influence of these competing forces is typically characterized by the dimensionless capillary number (N_{ca}), defined as the ratio of viscous to capillary forces. While various models have been developed to compute capillary numbers [1,2], Equation 1 represents the most widely adopted formulation.

$$N_{ca} = \frac{\mu_w * v}{\varphi * \gamma} \quad (1)$$

where,

μ_w: brine viscosity, Pa.s

γ : interfacial tension, mN/m

v : brine velocity, m/s

φ: porosity, fraction

The correlation between the capillary number and S_{nwr} is typically represented by a Capillary Desaturation Curve (CDC). Conventionally, for a water-wet system, the CDC is segmented into two distinct

* Corresponding author: djoshi1@uwyo.edu

regimes: a capillary-dominated region characterized by approximately constant residual non-wetting phase saturation, and a viscous-dominated region where fluid mobilization occurs (Figure 1(a)). The transition point between these regimes, termed the critical capillary number, is a pivotal parameter for gas sequestration estimations, generally observed within the range of 10^{-6} to 10^{-4}. While numerous studies [1–9] have documented this conventional CDC with two distinct regions and a critical capillary number, the majority have utilized synthetic porous media (i.e., glass beads or sand packs) [10–14] or homogeneous sandstone samples [2,7,15,16]. Furthermore, a notable characteristic of these studies is the utilization of liquid/liquid fluid systems [2,4,8,17,18].

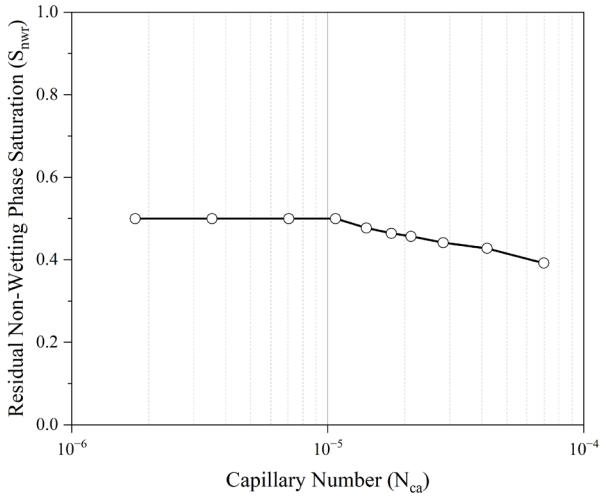

(a)

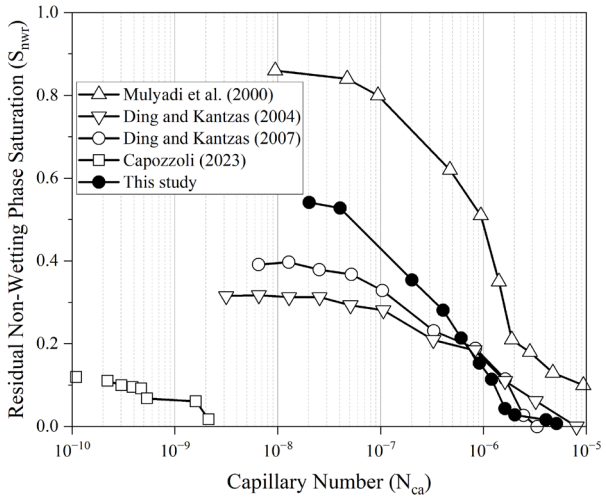

(b)

Fig. 1. (a) Conventional CDC for a homogeneous sandstone sample using liquid/liquid fluid system [19], (b) CDC reported for sandstones and carbonates using gas/liquid systems showing significant deviations from a conventional CDC [19–22].

However, to date, the relationship between capillary number and residual saturation in heterogeneous porous media and gas/liquid fluid systems is poorly understood. For example, studies employing carbonates [23,24], characterized by heterogeneity and dual porosity matrix, have reported CDCs that deviate significantly from the conventional model, exhibiting neither distinct capillary and viscous regions nor a discernable critical capillary number (Figure 1(b)). Several factors might impact this behavior in carbonates, including their broad and heterogeneous pore size distribution [7,10,16,25–28], elevated aspect ratios [23,24], and the Jamin effect [29]. Furthermore, the injection of gaseous phases introduces additional complexities [30]. Ding and Kantzas [19], using a series of experiments on sandstones and carbonates, reported that increasing waterflood flow rate within the capillary-dominated regime resulted in substantial reductions in residual gas saturation. This phenomenon was attributed to gas phase compressibility. Several other researchers [19,20,31–38] have reported similar observations, proposing diffusive gas transport, a process crucial for thermodynamic equilibrium, as a potential mechanism responsible for reduction in residual gas saturation.

To address the complexities of capillary desaturation within water-wet heterogeneous microporous carbonates, this study employs a multi-scale experimental methodology. Specifically, this research integrates macro-scale coreflooding experiments with high-resolution micro-scale investigations. The former was conducted under representative reservoir conditions using a high-pressure, high-temperature apparatus coupled with x-ray computed tomography. The latter leverages in-situ x-ray microcomputed tomography (micro-CT) to directly visualize and quantify pore-scale fluid displacement and fluid occupancy during the controlled flow of a N_2/brine system across various carbonates exhibiting different petrophysical characteristics. The latter approach aims to elucidate the pore-scale mechanisms governing non-wetting phase mobilization and entrapment. Subsequently, the insights gained from these pore-scale observations can be correlated with the macro-scale data, providing a comprehensive understanding of capillary desaturation processes relevant to field-scale gas injection and sequestration applications in complex carbonate reservoirs.

2 Rocks and Fluids

This study employed multiple carbonate rock samples from one outcrop (Estaillades) and two reservoir formations (Reservoir A and Reservoir B) to represent a range of petrophysical characteristics. A core plug (38 mm in diameter and 76 mm in length) was extracted from the outcrop rock block. The reservoir core plugs underwent in situ solvent cleaning followed by helium porosity and permeability measurements. Subsequent to routine core analysis, miniature core samples (8 mm in diameter, 66−76 mm long) were drilled from the outcrop core plug and reservoir core plug A for micro-scale coreflooding experiments. The core plug from Reservoir B was used for macro-scale coreflooding. Geometrical and petrophysical properties of the rock samples are

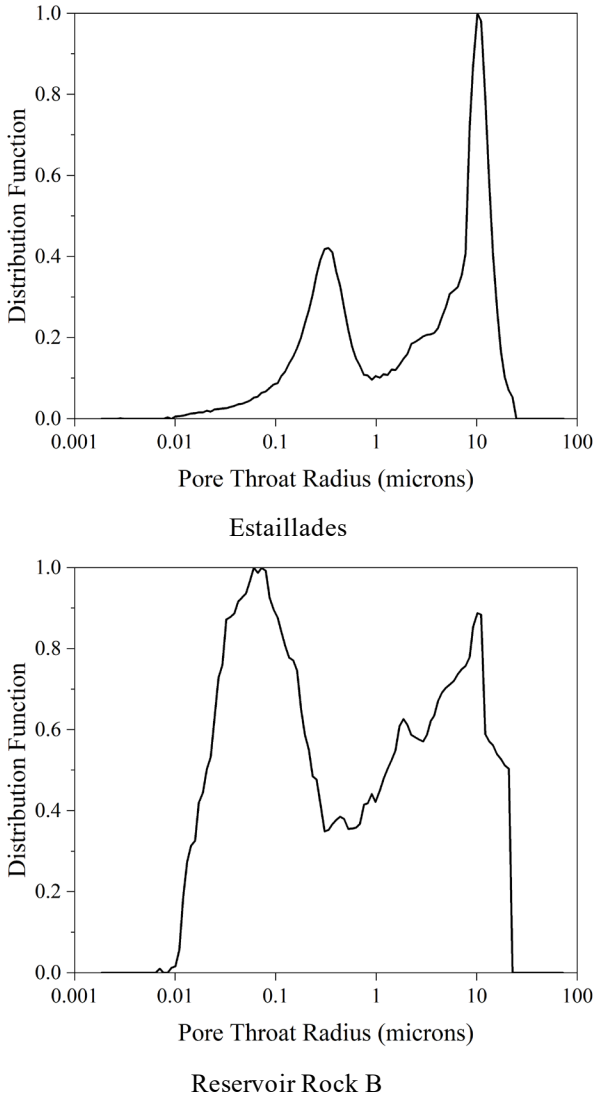

Fig. 2. Pore-throat size distributions obtained via MICP test for the outcrop sample and Reservoir Rock B used in this study

summarized in Table 1. Pore-throat radius distributions, determined on rock chips from the outcrop and reservoir rock B via mercury injection capillary pressure (MICP), are presented in Figure 2.

Table 1. Geometric and petrophysical properties of the miniature core samples and the core plug used in the coreflooding experiments.

Sample	Length (mm)	Diameter (mm)	X-ray-derived Porosity (%)	Brine Absolute Permeability (mD)
Estaillades	76.2	8.0	28.6	114.6
Reservoir miniature sample A	66.0	8.0	22.9	5.2
Reservoir core plug B	63.6	38.3	11.3	1.7

Nitrogen gas (N_2) was employed as the non-wetting phase across all experiments. For micro-scale analyses, two distinct brine compositions were used: a high-salinity brine (with 10 wt% NaI as dopant) for sub-resolution porosity characterization and a low-salinity brine (with 6 wt% NaI as dopant) for capillary desaturation curve generation. The outcrop sample used a synthetic brine doped with sodium iodide (NaI) for enhanced x-ray contrast. For reservoir rocks, formation brine was modified by substituting a portion of sodium chloride (NaCl) with NaI to optimize phase differentiation while maintaining the TDS of the formation brine. A high-salinity brine (with 12 wt% NaI as dopant) was used in the macro-scale experiment. Fluid properties for all experiments are summarized in Table 2. To mitigate potential matrix dissolution, the brines underwent pre-equilibration with rock chips prior to the flow experiment. Subsequent to equilibration, the brines were deaerated and filtered to eliminate any residual particulates.

Table 2. Properties of the fluids used in this study

Fluid	**Experiment Scale**	**Brine Composition**	**Density (g/ml)**	**Viscosity (cP)**	**Gas-brine IFT (mN/m)**
Nitrogen	Micro and Macro	-	0.11	0.02	57.11
Brine A	Micro	Formation brine with 10 wt% NaI	1.15	1.16	-
Brine B	Micro	Formation brine with 6 wt% NaI	1.12	0.80	-
Brine C	Macro	Formation brine with 12 wt% NaI	1.14	0.80	-

*Properties of Brine A were measured at 200 psi and ambient temperature. Properties of the remaining fluids were measured at 1,500 psi and 50°C. IFT was measured with respect to Brine B. More information about the composition of the formation brine can be found elsewhere [40].

3 Experimental Apparatus

Micro-scale fluid displacement experiments were conducted using a two-phase coreflooding system coupled with a micro-CT scanner. Macro-scale experiments employed a similar coreflooding setup integrated with a robotic X-ray scanner (Figure 3). The coreflooding apparatus, designed in a closed-loop configuration, comprised five dual-cylinder Quizix 5000 pumps, a suite of high-precision Rosemount differential pressure transducers, and a separator. Two of the pumps were used for gas and brine injection. The third pump received the effluents at constant pressure. Another pump maintained the pressure of the separator, while the last pump provided the confining pressure. All core samples were vertically positioned during the experiments. More details about the experimental setup can be found elsewhere [30].

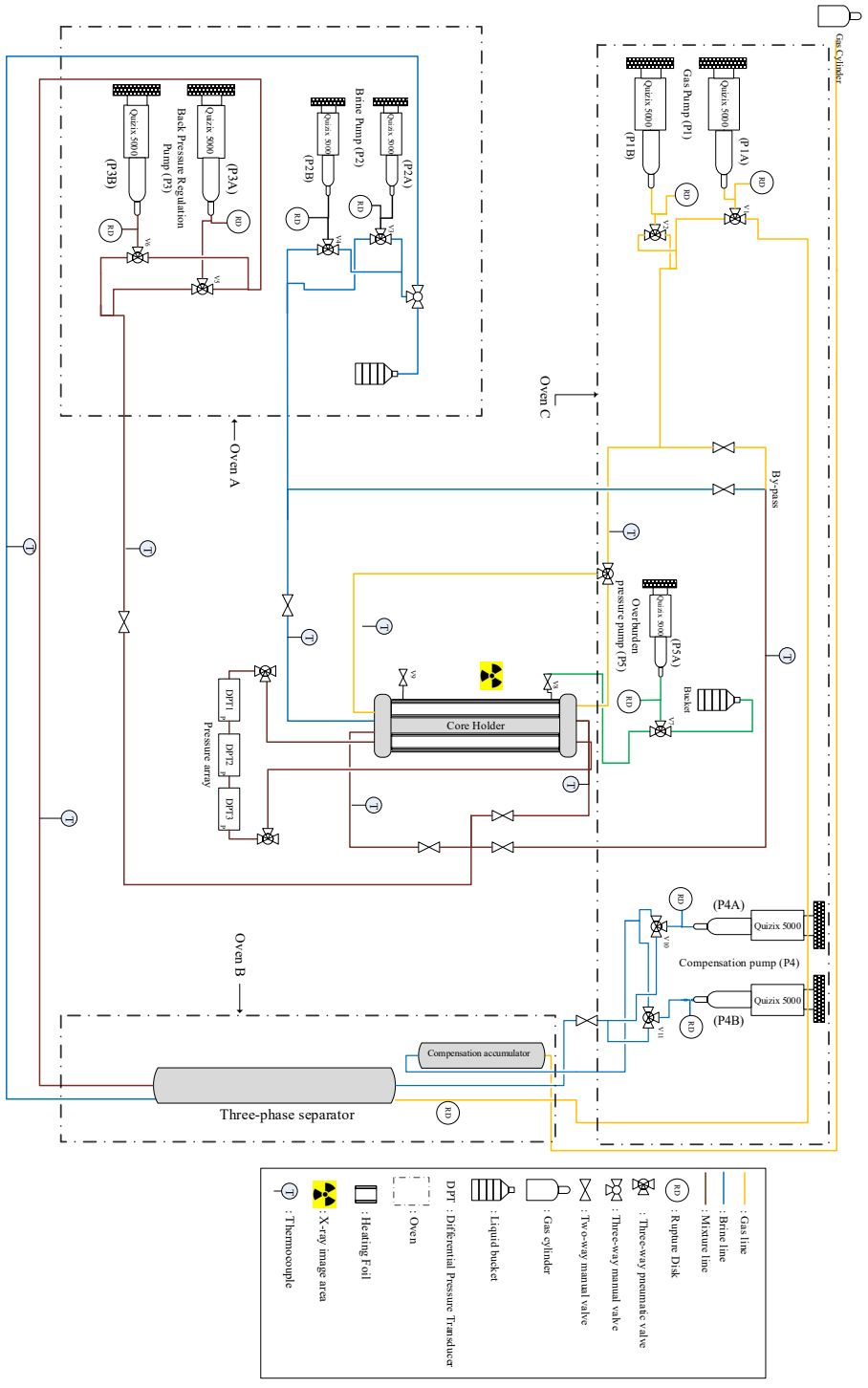

Fig. 3. Schematic representation of the experimental apparatus [39]. The X-ray imaging technique varied according to experimental scale: micro-CT for micro-scale analysis and robotic CT for macro-scale analysis.

4 Experimental Methodology

4.1 Micro scale

Precise quantification of micro-porosity is essential for the accurate determination of fluid saturation within heterogeneous microporous carbonate rocks. To this end, differential imaging micro-CT scanning, as described in [41], was employed to quantify sub-resolution porosity and accurately evaluate saturations. Upon mounting the core holder loaded with the rock sample, a dry reference scan was obtained. Subsequently, the rock sample was vacuum saturated with Brine A. Afterwards, Brine A reference scan was obtained, and sub-resolution porosity was computed by performing image analysis using Avizo 9.4.0. Brine A was then miscibly displaced with Brine B, and the system pressure and temperature were incrementally increased to 1500 psi and 50°C, respectively, while maintaining a net confining pressure of 500 psi. Upon reaching the desired experimental conditions, the core sample was isolated from the coreflooding apparatus, and fluids were circulated within the setup to ensure fluid equilibration and minimize mass transfer during the experiment. The non-equilibrated brine in the core sample was then miscibly displaced with the equilibrated brine, and another reference scan was acquired. N_2 was injected at a predetermined flow rate, which was subsequently increased to achieve the targeted initial water saturation. Furthermore, the direction of gas injection was reversed to optimize the displacement efficiency and to promote a more uniform saturation distribution throughout the sample. Following drainage, waterflooding was conducted at a flow rate corresponding to a capillary number of approximately 10^{-8}. The capillary number was subsequently increased by increasing the flow rate, and corresponding changes in saturation and fluid occupancies were recorded using micro-CT scans. Injection was halted upon reaching a steady-state condition in terms of differential pressure, after which the system was allowed to equilibrate before imaging commenced. Equation 1 was used to calculate capillary numbers. Two methodologies were used for fluid saturation determination: image segmentation-based and CT number-based. Detailed descriptions of these methodologies are available in [30].

4.2 Macro scale

At the macro scale, air and brine (Brine C) scans were obtained in addition to the methodology outlined in section 4.1. Two experiments (A and B) were performed on the same sample, with the second experiment (Experiment B) targeting a lower initial water saturation compared to the first one (Experiment A). Equations 2-4 [42] were used to compute porosity and fluid saturations.

$$\varphi = \frac{CT_{wc} - CT_{gc}}{CT_w - CT_g} \quad (2)$$

$$S_w = \frac{CT_c - CT_{gc}}{CT_{wc} - CT_{gc}} \quad (3)$$

$$S_g = 1 - S_w \quad (4)$$

where,

CT_{wc}, CT_{gc} represent CT numbers of the core fully saturated with brine and gas at the experimental conditions, respectively. CT_w, CT_g represent CT numbers of the fluids (brine and gas) (i.e., without the core) used in the experiment, respectively. CT_c, S_w, S_g refer to the CT number of the core containing two phases, brine saturation, and gas saturation, respectively.

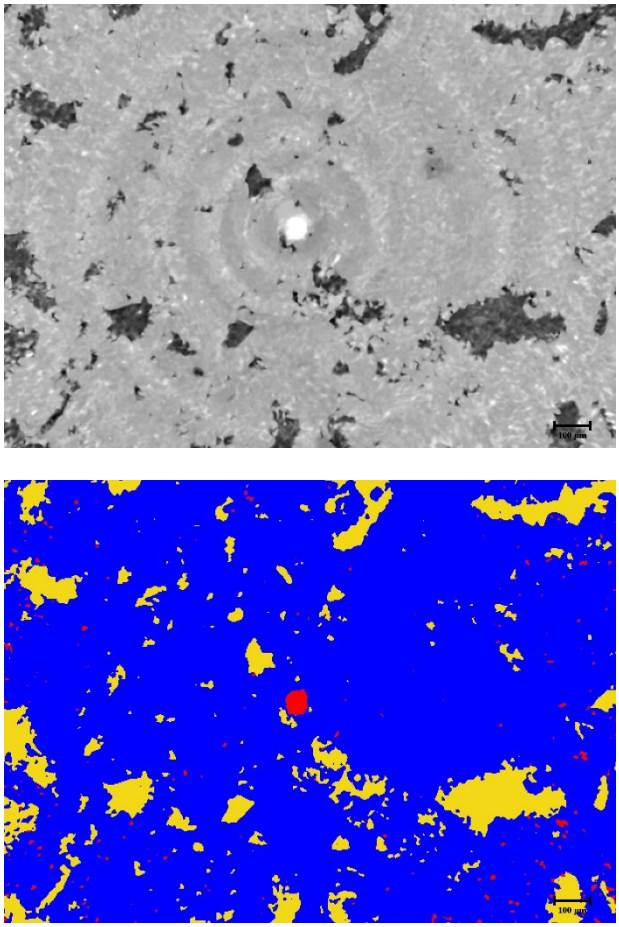

Fig. 4. Example of the differential imaging and processing methodology used in this study to obtain sub-resolution porosity (resolution = 2.79 µm). Top: grayscale image of Reservoir Sample A saturated with Brine A (gray: matrix, black: pore), and Bottom: the segmented image of the top grayscale one (red: matrix, blue: sub-resolution porous region, yellow: pore)

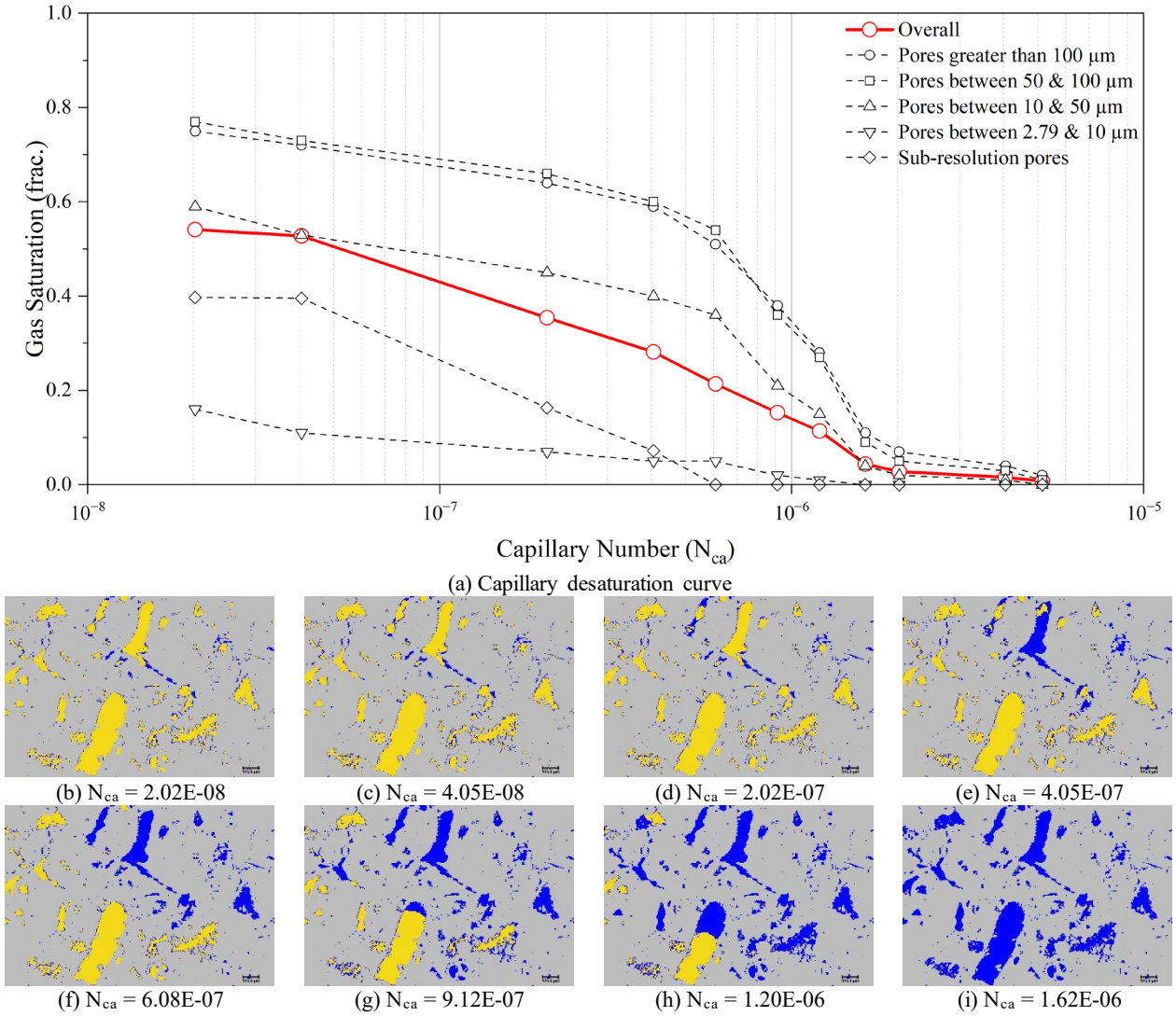

Fig 5. (a) CDC for Reservoir Sample A, showing desaturation profiles across various pore size groups. (b-i) Pore-scale fluid occupancy maps illustrating desaturation behavior as the capillary number increases during waterflooding (gray: matrix, blue: brine, yellow: gas).

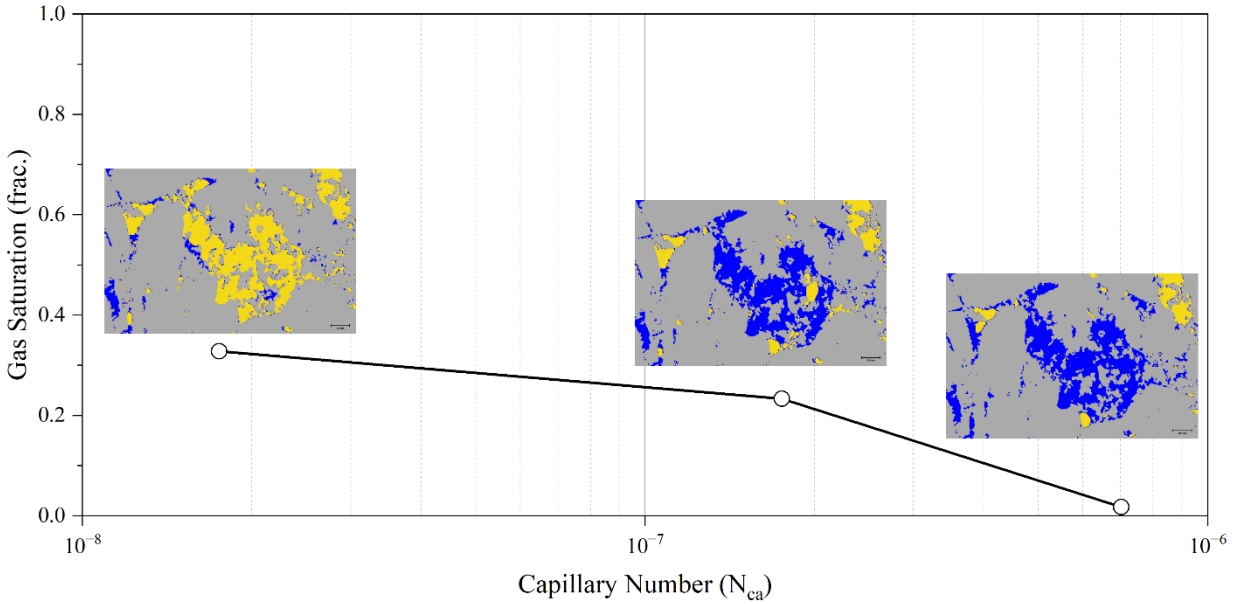

Fig. 6. CDC for the Estaillades rock sample along with pore-scale fluid occupancy maps illustrating desaturation behavior as the capillary number increases during waterflooding (gray: matrix, blue: brine, yellow: gas).

Table 3. Macro, sub-resolution, and total porosities of the carbonate samples determined using different techniques.

	Reservoir Sample A			Estaillades		
	Macro	Sub-resolution	Total	Macro	Sub-resolution	Total
Helium porosity (%)	-	-	22.19	-	-	29.72
Porosity from segmentation (%)	9.90	13.04	22.94	20.43	8.02	28.45
Porosity from MICP (%)	-	-	-	17.69	11.71	29.40

5 Results and Discussion

5.1 Micro scale

Precise evaluation and detailed characterization of sub-resolution porosity are crucial for producing dependable saturation measurements. To this end, we applied the methodology outlined by Lin et al. [41] and the analytical techniques detailed by Joshi et al. [30] to determine sub-resolution porosity for the two core samples used in this study. The results, along with a comparative analysis against helium porosimetry and mercury injection capillary pressure (MICP) data, are presented in Table 3. Figure 4 illustrates the characterization of sub-resolution porosity for Reservoir Sample A using micro-CT imaging.

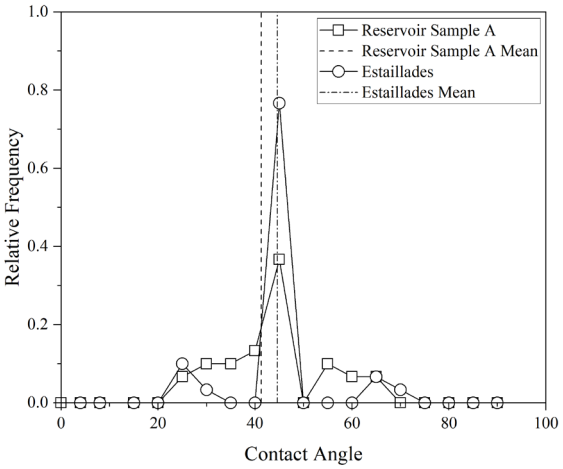

Fig. 7. Advancing contact angle distributions for Reservoir Sample A and the Estaillades sample measured in-situ using micro-CT images acquired during waterflooding.

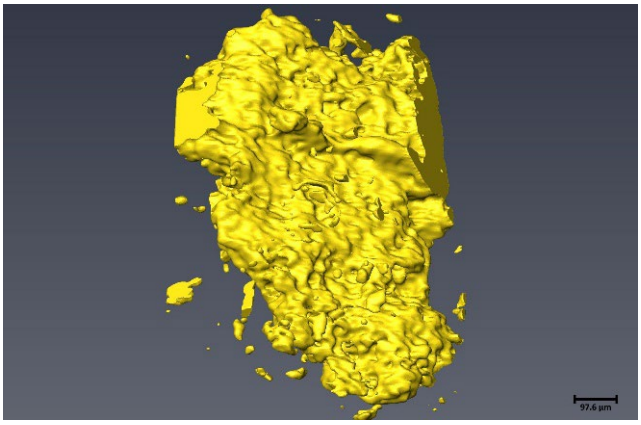

(a) N_{ca} = 2.02E-08

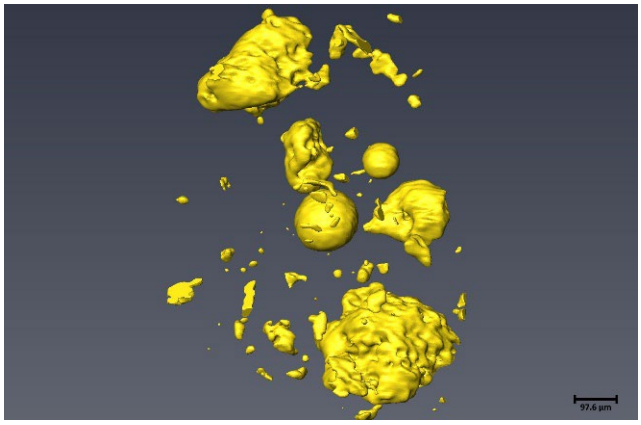

(b) N_{ca} = 2.02E-07

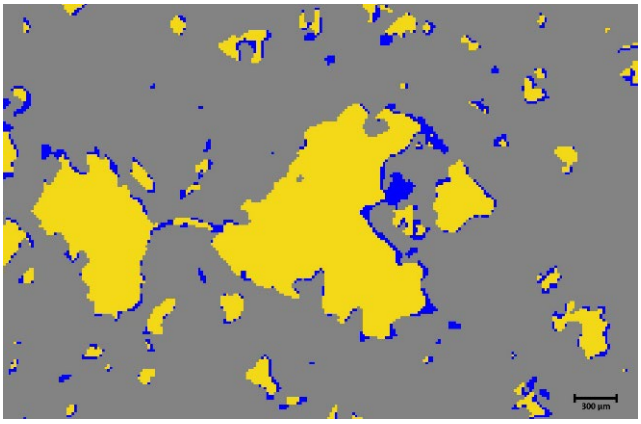

(c) N_{ca} = 2.02E-08

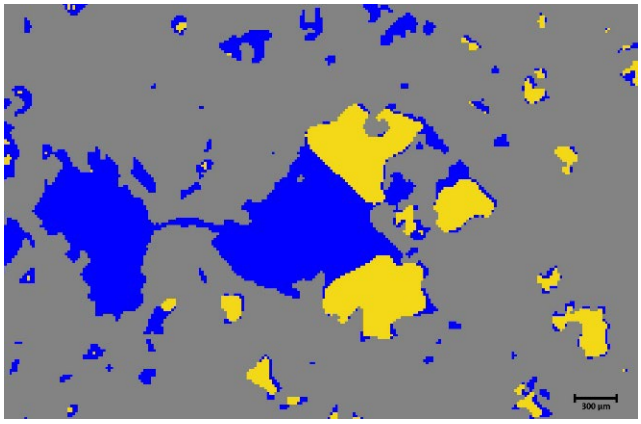

(d) N_{ca} = 2.02E-07

Fig. 8. Visualization of fragmentation of trapped globules in Reservoir Rock A in 3D (a-b) and 2D (c-d) due to increased capillary number during waterflooding (gray: matrix, blue: brine, yellow: gas).

Figures 5 and 6 exhibit the CDCs for Reservoir rock A and the Estaillades sample, respectively. Specifically, Figure 5(a) elucidates the desaturation behavior across a range of pore sizes in the reservoir specimen, demonstrating that desaturation occurred throughout the pore network rather than being confined to specific pore size domains. This global desaturation phenomenon was more remarkable in the macro-scale experiments (see Section 5.2). A notable observation from Figure 5(a) is the enhanced recovery and rapid desaturation in pores smaller than 10 microns. This is consistent with the established principle that, during waterflooding in a water-wet system, brine initially invades smaller pores, through displacement mechanisms such as piston-like events[43–49]. Correspondingly, Figures 5(b) through 5(i) depict pore-scale fluid occupancy maps during the waterflooding process for Reservoir rock A, while Figure 6 presents those for the Estaillades sample. The observed differences in desaturation trends between the two samples can be linked to variations in pore space properties such as pore geometry, aspect ratio, coordination number [23], and pore size distributions [10,24]. These properties critically influence flow behavior through changes in pore connectivity and fluid displacement efficiency within each rock. Carbonates, such as those used in this study, are inherently heterogeneous in terms of pore-scale structure and property distribution, which manifests in the variability observed in the desaturation behavior of the samples.

The literature suggests that in non-water-wet cases, a continuous decrease in trapped gas saturation with increasing capillary number is prevalent [10,50]. Such cases lack a distinct critical capillary number as well as well-defined capillary dominated and viscous dominated regimes, such as those shown in Figures 5 and 6. Therefore, to ascertain the water wetness of Reservoir Sample A and the Estaillades sample, in-situ advancing contact angles were measured using the micro-CT images acquired during waterflooding experiments (see Figure 7). The contact angle distributions of both core samples indicated water-wet conditions.

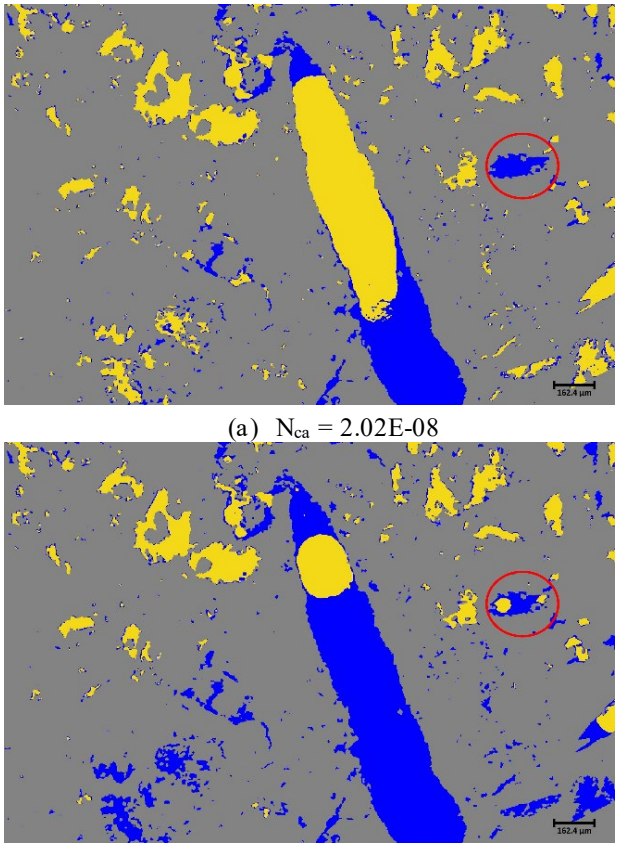

(a) N_{ca} = 2.02E-08

(b) N_{ca} = 2.02E-07

Fig. 9. Cross-sectional views of pore-scale occupancy showing trapped gas mobilization (red circles) in initially brine filled pore in Reservoir Rock A due to increased capillary number during waterflooding (gray: matrix, blue: brine, yellow: gas).

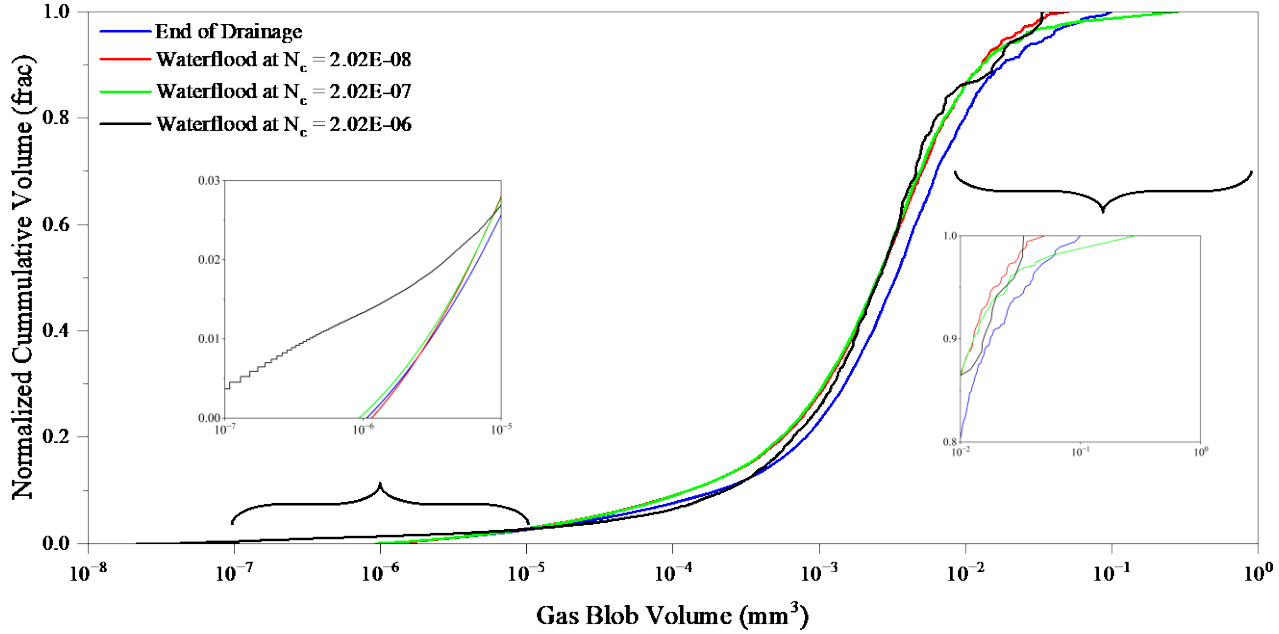

Fig. 10. Cluster analysis applied to trapped gas clusters, illustrating variations across sequential waterflood steps.

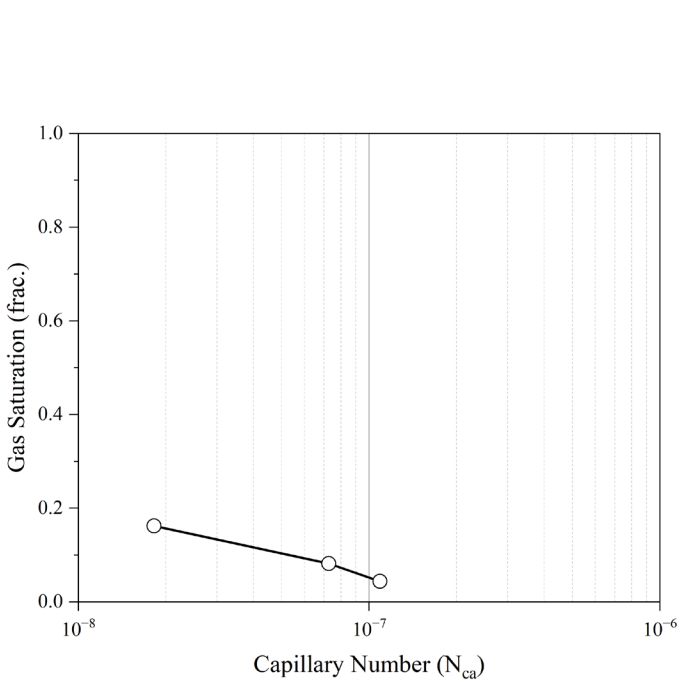

(a)

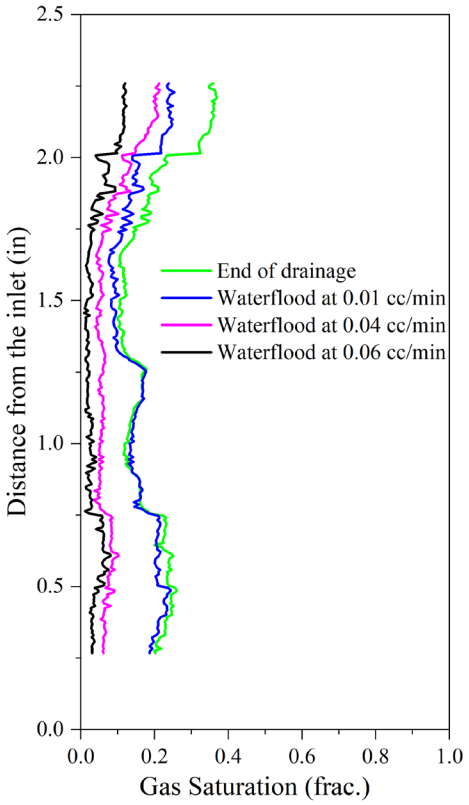

(b)

Reservoir Sample B Experiment A				
Step	0.31 in from inlet	0.94 in from inlet	1.18 in from inlet	1.97 in from inlet
Drainage	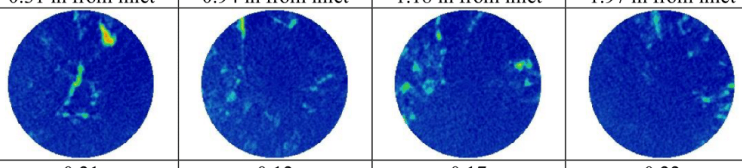			
Gas saturation (frac.)	0.21	0.12	0.17	0.22
Waterflood @ 0.01 cc/min	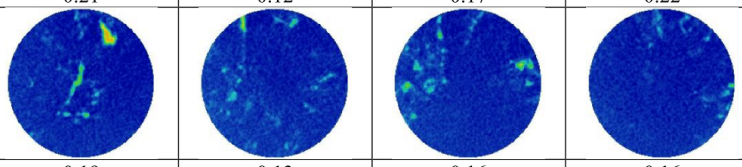			
Gas saturation (frac.)	0.19	0.13	0.16	0.16
Waterflood @ 0.4 cc/min	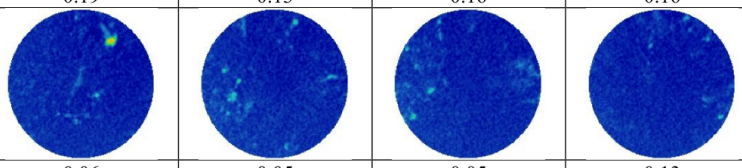			
Gas saturation (frac.)	0.06	0.05	0.05	0.13
Waterflood @ 0.6 cc/min	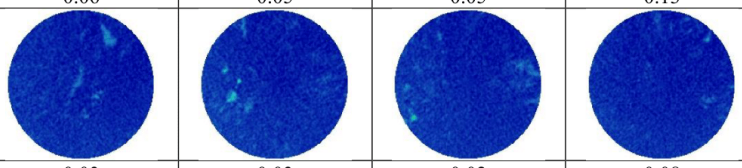			
Gas saturation (frac.)	0.03	0.03	0.02	0.08

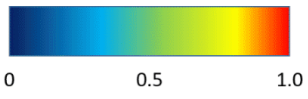

(c)

Fig. 11. (a) CDC, (b) gas saturation distribution across the core sample at different brine flow rate, and (c) CT image sequences illustrating fluid occupancy at key experimental intervals for Experiment A on Reservoir Sample B.

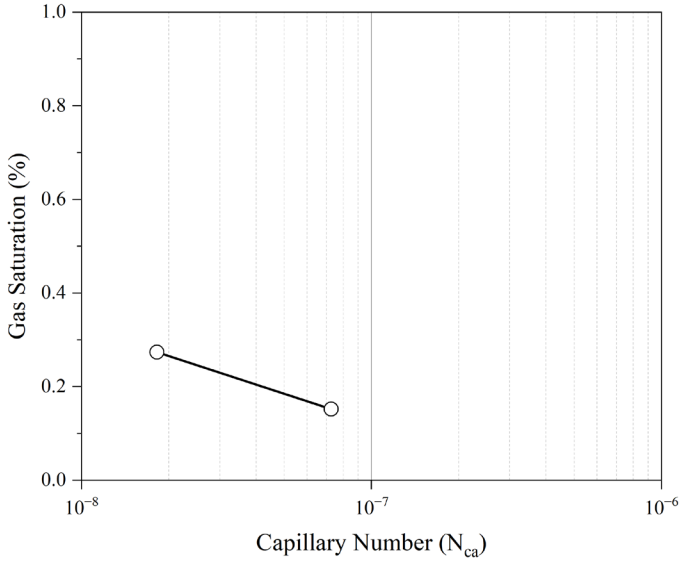

(a)

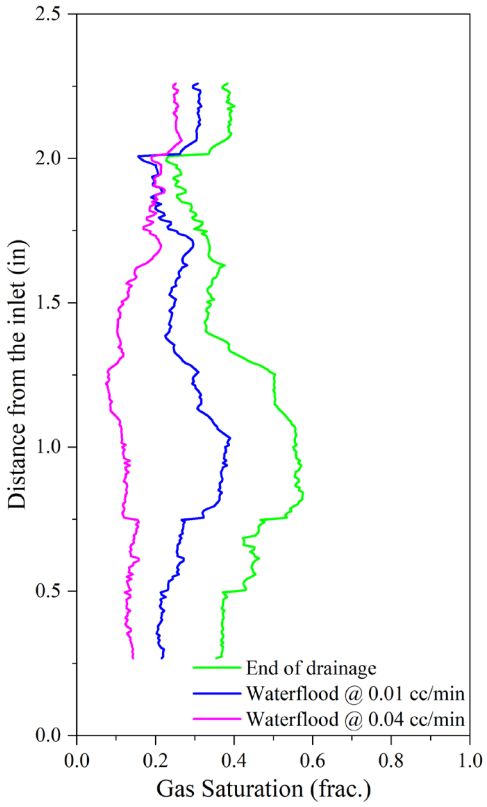

(b)

Reservoir Sample B Experiment B				
Step	0.31 in from inlet	0.94 in from inlet	1.18 in from inlet	1.97 in from inlet
Drainage	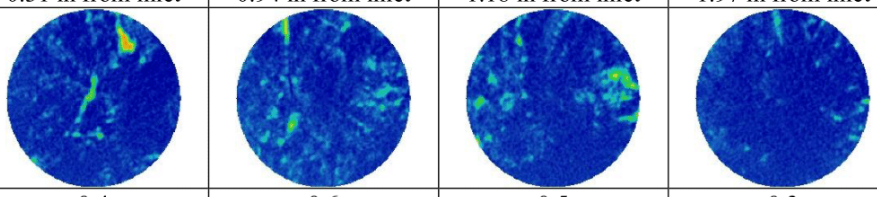			
Gas saturation (frac.)	0.4	0.6	0.5	0.3
Waterflood @ 0.01 cc/min	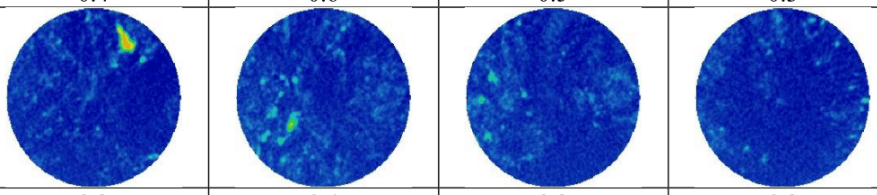			
Gas saturation (frac.)	0.2	0.4	0.3	0.3
Waterflood @ 0.4 cc/min	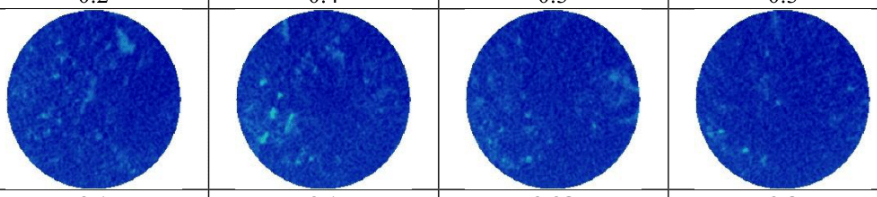			
Gas saturation (frac.)	0.1	0.1	0.08	0.2

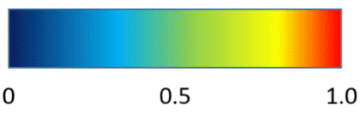

(c)

Fig. 12. (a) CDC, (b) gas saturation distribution across the core sample at different brine flow rate, and (c) CT image sequences illustrating fluid occupancy at key experimental intervals for Experiment B on Reservoir Sample B.

In water-wet systems, capillary trapping is controlled by snap-off events. Conventionally, trapped saturation remains relatively constant until the critical capillary number (approximately 10^{-6} to 10^{-4} depending on the porous medium) is attained, signifying the transition to viscous dominant regime. Viscous forces facilitate the mobilization and production of trapped globules through ganglion dynamics (fragmentation, coalescence, and displacement) due to increased pressure gradients. However, we observed mobilization and production of trapped globules at significantly lower capillary numbers in our experiments, a trend also observed in several studies [10,19–24]. The pore-scale fluid occupancy maps demonstrated the occurrence of two distinct pore-level events within the capillary-dominated regime: trapped globule fragmentation (Figure 8), as well as bubble mobilization (even in the brine-saturated pores) (Figure 9(a) and 9(b)).

After the trapped ganglia are fragmented, they are mobilized when the applied drag force exceeds a threshold value defined by Taber et al. [8]. Although the authors presented an equation for the threshold drag force in liquid/liquid systems (Eq. 5, where μ_o refers to oil viscosity), the application of this equation to gas/liquid systems suggests that the threshold is easily surpassed, even under low-capillary number conditions (as in this study).

$$\frac{\Delta P}{L\sigma} = 1.8 + 0.1 * \mu_o - |0.18 - 0.03 * \mu_o| \quad (5)$$

where ΔP is the pressure drop across distance L, and σ is the IFT between the fluid phases.

To probe the occurrence of fragmentation and mobilization in our experiment, we analyzed the trapped gas clusters at the end of each waterflood stage. Figure 10 demonstrates an increased contribution of smaller clusters to the total trapped non-wetting phase volume with increasing capillary number, consistent with the fragmentation observed in the fluid occupancy maps. Interestingly, in some cases, the volume of the largest trapped cluster increased with capillary number (e.g., between $N_{ca} = 2.02\times10^{-8}$ and 2.02×10^{-7}), contrary to expectation. This behavior is caused by mobilization of smaller globules and their coalescence with large, trapped gas clusters in larger pores [2], as shown in Figure 9(b), resulting in clusters with increased volume before they eventually break apart under higher pressure gradients at increased capillary numbers.

5.2 Macro scale

In addition to the micro-scale experiments described previously, we performed two experiments (A and B) at the macro scale on another core sample, Reservoir Sample B. The second macro-scale experiment (Experiment B) targeted a lower initial water saturation compared to the first one (Experiment A). The results for both experiments are shown in Figures 11 and 12, respectively.

The CDCs presented in Figures 11 and 12 illustrate remarkable desaturation within the capillary-dominated regime, a finding further substantiated by the CT images. The reduction in gas saturation, measured along the entire length of the sample in Experiment A and within its 0.5 to 1.5 inches (from the inlet) segment in Experiment B, is indicative of fragmentation and mobilization of trapped ganglia. This is supported by the in-situ evidence presented in section 5.1. The slight elevation in gas saturation recorded between 1.75 and 2 inches during Experiment B is a result of fluid mobilization and redistribution, as discussed earlier.

6 Conclusions

This study investigated capillary desaturation behavior of a gas/brine system in heterogeneous microporous carbonate rocks using micro- and macro-scale flow experiments. The experiments were conducted using high-pressure, high-temperature coreflooding apparatuses integrated with X-ray imaging equipment. Carbonate rock samples (outcrop and reservoir samples), exhibiting varied petrophysical properties, were employed in the experiments. Following the establishment of initial water saturation (S_{wi}) via drainage, waterflood was performed with systematically increased flow rates, and the corresponding saturation changes were recorded. The key findings are:

1. This study revealed a continuous decrease in trapped gas saturation with increasing waterflood flow rate, even within the capillary-dominated regime ($N_{ca} < 10^{-6}$).
2. Differential imaging techniques were employed at the micro-scale to accurately quantify sub-resolution microporosity and evaluate its influence on trapped gas desaturation.
3. Both pore-scale fluid occupancy maps and the generated capillary desaturation curve demonstrates the absence of a distinct critical capillary number or separate capillary- and viscous-dominated regimes in gas-liquid systems in carbonates.
4. Micro-scale experiments revealed trapped globule fragmentation and mobilization as the two primary displacement mechanisms responsible for the desaturation behavior observed.
5. Macro-scale observations aligned with pore-scale findings, further corroborating the observed desaturation behavior and the above proposed physics.

We gratefully acknowledge the financial support of Abu Dhabi National Oil Company and the University of Wyoming.

References

1. R.G. Larson, H.T. Davis, L.E. Scriven, Chem. Eng. Sci. **36**, 75 (1981)
2. A.I.A. Mohamed, M. Khishvand, M. Piri, Adv. Water Resour. **144**, 103702 (2020)

3. F.A.L. Dullien, I.F. MacDonald, SPE J. **16**, 7 (1976)
4. J.J. Stosur, J. Taber, J. Pet. Technol. **28**, 865 (1976)
5. W.R. Foster, J. Pet.Technol. **25**, 205 (1973)
6. J.C. Melrose, J. Can. Pet. Technol. **13** (1974)
7. A, Abrams, SPE J. **15**, 437 (1975)
8. J.J. Taber, SPE J. **9**, 3 (1969)
9. T.F. Moore, R.L. Slobod, *Fall Meeting of the Petroleum Branch of AIME (SPE)* (1955)
10. H. Tie, N.R. Morrow, *IPTC* (2005)
11. B.Y. Jamaloei, F. Ahmadloo, R. Kharrat, Fluid Dyn. Res. **42**, 55505 (2010)
12. F.A.L. Dullien, G.K. Dhawan, N. Gurak, L. Babjak, SPE J. **12**, 289 (1972)
13. L. Anton, R. Hilfer, Phys. Rev. E. **59**, 6819 (1999)
14. N.R. Morrow, I. Chatzis, J.J. Taber, SPE Reservoir Eng. **3**, 927 (1988)
15. I. Chatzis, N.R. Morrow, SPE J. **24**, 555 (1984)
16. B. Cheng, J. Li, S. Jiang, C. Lu, H. Su, F. Yu, J. Hanqiao, Energies **14**, 3057 (2021)
17. S.P. Gupta, S.P. Trushenski, SPE J. **19**, 116 (1979)
18. M. Khishvand, I.O. Kohshour, A.H. Alizadeh, M. Piri, S. Prasad, Fuel **250**, 117 (2019)
19. M. Ding, A. Kantzas, J. Can. Pet. Technol. **46** (2007)
20. H. Mulyadi, R. Amin, T. Kennaird, G. Bakker, I. Palmer, D.V. Nispen, *International Oil and Gas Conference and Exhibition in China, SPE* (2000)
21. M. Ding, A. Kantzas, *Canadian International Petroleum Conference* (2004)
22. P. Capozzoli, *Politecnico di Torino* (2023)
23. J. Kamath, F. Nakagawa, R. Meyer, S. Kabir, R. Hobbet, *SCA* (2001)
24. V.H. Nguyen, A.P. Sheppard, M.A. Knackstedt, W.V. Pinczewski, J. Pet. Sci. Eng. **52**, 54 (2006)
25. Y. Li, Y. Yang, M. Dong, C. Liu, S. Iglauer, L. Kang, J. Yao, K. Zhang, H. Sun, L. Zhang, SPE J. **27**, 1895 (2022)
26. E.J.L. du Prey, SPE J. **13**, 39 (1973)
27. G.L. Stegemeier, AIChe Symposium, 55 (1977)
28. R.K. Manning, *University of Texas at Austin* (1983)
29. J. Kamath, E.F. deZabala, R.E. Boyer, SPE Form. Eval. 10, 4 (1995)
30. D. Joshi, R. Ali, Z. Qin, A.H. Alizadeh, M. Piri, *ADIPEC* (2024)
31. T.M. Geffen, D.R. Parrish, G.W. Haynes, R.A. Morse, J. Pet. Technol. **4**, 29 (1952)
32. D.K. Keelan, V.J. Pugh, SPE J. 15, 149 (1975)
33. J. Delclaud, *SCA* (1991)
34. K.M. Adam, G.L. Bloomsburg, A.T. Corey, Water Resour. Res. **5**, 840 (1969)
35. G.L. Bloomsburg, A.T. Corey, *Colorado School of Mines* (1964)
36. K.M. Adam, A.T. Corey, *Colorado School of Mines* (1968)
37. J.E. Christiansen, Soil Sci. **58**, 355 (1944)
38. A. Kantzas, M. Ding, J. Lee, SPE Reservoir Eval. Eng. **4**, 467 (2001)
39. M. Piri, *WO 2012/082797 A1* (2012)
40. S. Masalmeh, A. Al-Mesmari, S.A. Farzaneh, M. Sohrabi, *ADIPEC* (2022)
41. Q. Lin, Y. Al-Khulaifi, M.J. Blunt, B. Bijeljic, Adv. Water Resour. **96**, 306 (2016)
42. A.H. Alizadeh, M. Piri, Water Resour. Res. **50**, 1636 (2014)
43. S.M. Fullmer, S.A. Guidry, J. Gournay, E. Bowlin, G. Ottinger, A.M. Al Neyadi, G. Gupta, B. Gao, E. Edwards, *IPTC* (2014)
44. A. Mehmani, M. Prodanović, Adv. Water Resour. **63**, 104 (2014)
45. J.G. Kralik, L.J. Manak, G.R. Jerauld, A.P. Spence, *SPE ATCE* (2000)
46. T. Bultreys, J.V. Stappen, T. D. Kock, W.D. Boever, M.A. Boone, L.V. Hoorebeke, V. Cnuddle, J. Geophys. Res. Solid Earth **121**, 7929 (2016)
47. S, Fullmer, H. Al Qassab, A. Buono, B. Gao, B. Kelley, P.J. Moore, SEPM, 268 (2019)
48. G. Zhang, M. Regaieg, M.J. Blunt, B. Bijeljic, J. Hydrol. (Amst) **625**, 130022 (2023)
49. N. Alyafei, M.J. Blunt, Adv. Water Resour. **90**, 36 (2016)
50. K.J. Humphry, B.M.J.M. Suijkerbuijk, H.A. van der Linde, S.G.J. Pieterse, S.K. Masalmeh, Petrophysics **55**, 313 (2014)